Volume 18
Number 5
5 February 2026
Pages 2293-2874

Nanoscale

rsc.li/nanoscale

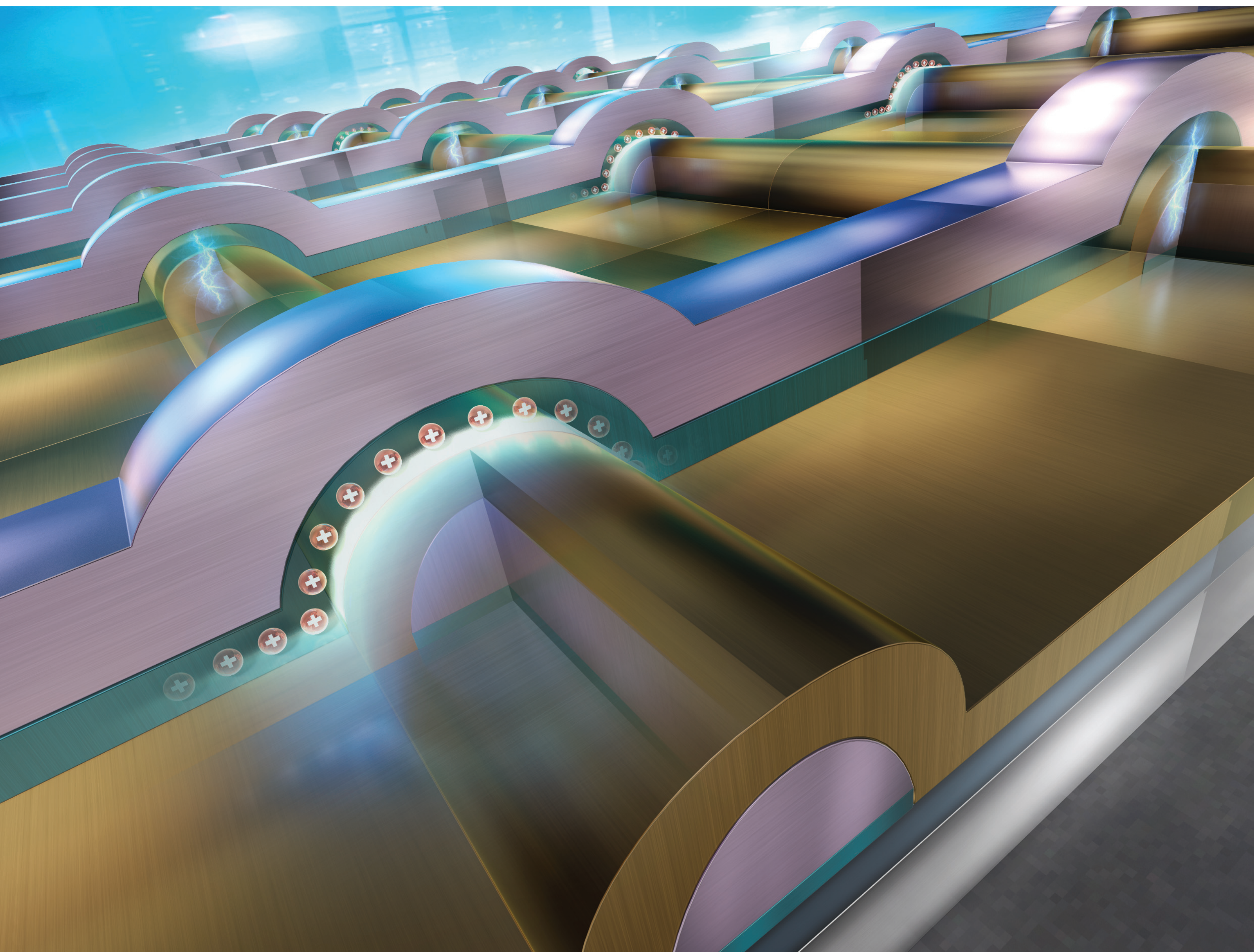

ISSN 2040-3372

ROYAL SOCIETY OF CHEMISTRY

PAPER
Yutaka Majima *et al.*
High-resistance-state tunneling in 25 nm TiO_x/Y-doped HfO_2/Pt nanocrossbar ferroelectric tunnel junctions

NCNST

Nanoscale

ROYAL SOCIETY OF CHEMISTRY

PAPER

View Article Online
View Journal | View Issue

Cite this: *Nanoscale*, 2026, **18**, 2525

High-resistance-state tunneling in 25 nm TiO_x/Y-doped HfO_2/Pt nanocrossbar ferroelectric tunnel junctions

Zhongzheng Sun,[a] Yoshiko Nakamura,[b] Kazuki Okamoto, [b] Seiichiro Izawa, [a] Hiroshi Funakubo [b] and Yutaka Majima *[a]

We report nanocrossbar-type ferroelectric tunnel junctions (FTJs) with a Ti/TiO_x/7% yttrium-doped HfO_2 (YHO_7)/Pt structure integrated on thermally oxidized Si substrates, which exhibit clear direct tunneling conduction even in the high-resistance state (HRS) and a tunneling electroresistance ratio exceeding 10^3. The nanocrossbar FTJs were fabricated using a double-exposure electron-beam lithography (EBL) process with lateral dimensions scaled down to 25 nm. The temperature dependence of the TER effect measured at 9 and 300 K confirms that both low- and high-resistance states are dominated by the direct tunneling conduction. A maximum TER ratio of 2.2×10^3 was obtained in a 3 nm-thick YHO_7 nanocrossbar FTJ with an effective area of 26×24 nm^2. The FTJ area was reduced from 42 000 to 255 nm^2, and the scaling behavior of the TER effect in 3 nm-thick YHO_7 devices closely resembles that in 2 nm-thick devices. The OFF-state current decreased with a slope of 1.1 between 42 000 and 2600 nm^2, followed by a steeper reduction below 2600 nm^2, whereas the ON-state current decreased more gradually with a slope of 0.30. These contrasting area dependences are attributed to the suppression of leakage pathways along grain boundaries in the OFF state and to uniformly aligned remanent polarization within a limited number of grains in the ON state. The demonstrated nanocrossbar FTJs highlight a promising route toward high-density, energy-efficient, and CMOS-compatible integration of ferroelectric memory.

Received 23rd September 2025,
Accepted 11th December 2025

DOI: 10.1039/d5nr04010h

rsc.li/nanoscale

Open Access Article. Published on 02 ledna 2026. Downloaded on 21.05.2026 4:19:18.
This article is licensed under a Creative Commons Attribution 3.0 Unported Licence.

Introduction

The rapid advancement of artificial intelligence (AI) and neuromorphic computing has increased the demand for memory devices that are not only non-volatile but also exhibit fast switching speeds, high scalability, compatibility with complementary metal–oxide semiconductor (CMOS) technology, and low power consumption—key attributes for integrating memory and computation in AI-driven systems.[1–5] Ferroelectric materials have emerged as promising candidates for non-volatile memory applications owing to their electrically switchable spontaneous polarization.[6–8] Among the most investigated device architectures are ferroelectric field-effect transistors (Fe-FETs) and ferroelectric tunnel junctions (FTJs). The FTJ is a two-terminal, non-volatile memory element that enables fast switching, long endurance, non-destructive readout, and a high ON/OFF resistance ratio, making it well-suited for next-generation storage-class memory.[8–11] It typically consists of a metal/ferroelectric/metal heterostructure, in which the incomplete screening of polarization charges by the electrodes and the use of ultrathin ferroelectric barriers enable modulation of the tunneling barrier height and width through polarization switching.[10,12,13] This modulation results in a change in tunneling resistance between low-resistance (ON) and high-resistance (OFF) states, a phenomenon known as the tunneling electroresistance (TER) effect.[14]

Esaki *et al.* first proposed the FTJ concept in 1971.[15] Realization of FTJs requires ultrathin ferroelectric barriers that support direct tunneling. However, as the ferroelectric layer thickness is scaled down to the nanometer regime, size effects arising from grain size, domain structure, lattice strain, and surface energy can degrade or suppress ferroelectricity.[16,17] When combined with depolarization fields, the size effects often lead to a critical thickness below which ferroelectricity is lost.[18,19] Contreras *et al.* reported early FTJ behavior in a 6 nm-thick $PbZr_{0.52}Ti_{0.48}O_3$ film sandwiched between $SrRuO_3$ and Pt electrodes,[20] marking the beginning of substantial FTJ research based on perovskite ferroelectrics.[21–23] However, perovskite-based FTJs face challenges such as size-dependent ferroelectric degradation, high crystallization temperatures, and poor CMOS compatibility.[23]

[a]*Materials and Structures Laboratory, Institute of Integrated Research, Institute of Science Tokyo, Yokohama, 226-8503, Japan. E-mail: majima@msl.titech.ac.jp*
[b]*School of Materials and Chemical Technology, Institute of Science Tokyo, Yokohama, 226-8503, Japan*

This journal is © The Royal Society of Chemistry 2026

Open Access Article. Published on 02 ledna 2026. Downloaded on 21.05.2026 4:19:18.
This article is licensed under a Creative Commons Attribution 3.0 Unported Licence.

Hafnium oxide (HfO_2) has emerged as a high-k dielectric widely adopted in industry as a gate insulator, offering superior compatibility with CMOS platforms.[24] In 2011, Böscke *et al.* discovered that Si-doped HfO_2 exhibits ferroelectric behavior, paving the way for doped-HfO_2-based ferroelectric thin films.[25] Ferroelectricity in HfO_2 is associated with the non-centrosymmetric orthorhombic phase ($Pca2_1$), which can be stabilized through chemical doping, interface engineering, or thermal treatment.[25–28] Unlike perovskite ferroelectrics, HfO_2-based ferroelectrics exhibit mitigated size effects, owing to their fluorite-derived structure that reduces lattice distortions and surface-related instabilities at single nanoscale thickness.[29] These features, combined with a high dielectric constant, make doped-HfO_2 a strong candidate for use as a tunneling barrier in FTJs.

We recently reported that Y_2O_3 is a promising dopant for HfO_2 due to its low sensitivity to surface energy, a feature not commonly observed in other doped-HfO_2 systems.[30] Stable remanent polarization was confirmed in nanometer-thick Y_2O_3-doped HfO_2 films grown directly on $Pt/Ti/SiO_2/Si$ substrates. Furthermore, we demonstrated the room-temperature growth of polycrystalline 7% Y-doped HfO_2 (YHO_7) by RF magnetron sputtering, which exhibits clear ferroelectric behavior.[31] These results highlight YHO_7 as a viable candidate for tunneling barriers in FTJ applications.

TER effects have been demonstrated at lateral dimensions below 100 nm, aligning with the requirements for high-density FTJ memory integration.[32–35] For instance, conductive atomic force microscopy (c-AFM) studies have shown TER ratios exceeding 10^3 in perovskite FTJs.[32–34] Abuwasib *et al.* employed hydrogen silsesquioxane (HSQ) planarization to fabricate perovskite-based FTJs with a TER ratio of 125.[35]

Recently, we demonstrated robust Pt nanogap electrodes with 10 nm linewidths by electron-beam lithography (EBL)[36] and achieved in-plane ferroelectric memory operation in 100 nm channel-length α-In_2Se_3 devices on SiO_2/Si substrates.[37] For practical high-density memory integration, FTJ fabrication directly on SiO_2/Si substrates *via* streamlined processes is highly desirable. The crossbar structure provides a compact and regular array format that facilitates two-terminal addressing and high cell density, making it particularly suitable for scalable ferroelectric memory architectures.

In this study, we demonstrate scalable nanocrossbar FTJs fabricated through a double-exposure EBL process. The devices consist of Ti/TiO_x electrode/YHO_7 (2 and 3 nm)/Pt stacks on thermally oxidized Si substrates, with lateral dimensions down to 25 nm. The temperature dependence of the TER effect at 9 and 300 K confirms tunneling conduction in both the low- and high-resistance states. A maximum TER ratio of 2.2×10^3 is achieved in a 3 nm YHO_7 nanocrossbar FTJ with an effective area of 26×24 nm^2, and the area scaling of the TER effect is systematically investigated. These results highlight the potential of nanocrossbar FTJs for high-density, energy-efficient, and CMOS-compatible, scalable integration of ferroelectric memory.

Results and discussion

Characterization of ferroelectricity of YHO_7

The ferroelectric properties of an ultrathin YHO_7 film, suitable for enabling direct tunneling, were investigated using piezoresponse force microscopy (PFM).[38] A 3 nm YHO_7 film was deposited on a $Pt/Ti/SiO_2/Si$ substrate by radio-frequency magnetron sputtering at room temperature. The local PFM amplitude and phase contrast images, as well as the film's hysteresis loops, are shown in Fig. 1.

A −2.5 V pulse was first applied at the outer square (6 × 6 μm), and, subsequently, a 2.5 V pulse was applied at the inner square (2 × 2 μm^2). Box-in-box PFM amplitude and phase contrast images are shown in Fig. 1a and b, respectively.

A butterfly-shaped amplitude loop and a phase hysteresis loop with 180° shift were observed (Fig. 1c and d), confirming ferroelectric switching behavior in 3 nm-thick YHO_7. It was noted that the 3 nm YHO_7 film exhibited clear amplitude and phase hysteresis loops from the first cycle of voltage sweep, indicating the presence of stable spontaneous polarization in the as-deposited state.

Fabrication of scalable nanocrossbar FTJs

Straightforward fabrication processes were developed to prepare 25 nm squared nanocrossbar $Ti/TiO_x/YHO_7/Pt$ FTJs using double-exposure EBL on SiO_2/Si substrates. A top-view SEM image of the 25 nm squared nanocrossbar $Ti/TiO_x/YHO_7/Pt$ FTJs is shown in Fig. 2a. In this nanocrossbar FTJ, the bottom Pt and top Ti/TiO_x electrode widths are 26 nm and 24 nm, respectively, yielding an effective junction area of 624 nm^2.

Fig. 2b shows a cross-sectional SEM image of the $Ti/TiO_x/YHO_7/Pt$ structure with false coloring applied to the Ti/TiO_x (blue), YHO_7 (light ochre), and Pt (purple) layers. The bottom Pt nanowire electrode, composed of Pt (6 nm)/Ti (1 nm adhesion layer), was prepared by EBL, and then annealed in 3% H_2/Ar at 550 °C for 5 min. The cross-sectional shape of the bottom Pt nanowire electrode transformed from a rectangle to a semicircular arch, as shown in the cross-sectional SEM image in Fig. 2b. During this annealing process, the Pt crystallinity improved.[39,40]

YHO_7 films with thicknesses of 2 and 3 nm were subsequently deposited by RF magnetron sputtering onto the curved bottom Pt nanowire electrodes.[31] As observed in Fig. 2b, the semicircular Pt geometry facilitates conformal deposition of ultrathin YHO_7 films, supporting the formation of a FTJ structure without short-circuiting. The top Ti nanowire electrode, consisting of Pt (10 nm)/Ti (3 nm), was prepared by overlay EBL.

Fig. S1 shows a cross-sectional bright-field TEM (BF-TEM) image, and Fig. S2 presents the corresponding EDS elemental mapping (SI). The cross-sectional TEM image is consistent with the FE-SEM image in Fig. 2b, and the EDS elemental mapping confirms that the layer sequence corresponds to a $Ti/TiO_x/YHO_7/Pt$ stack structure shown with false coloring in Fig. 2b.

Open Access Article. Published on 02 ledna 2026. Downloaded on 21.05.2026 4:19:18.
This article is licensed under a Creative Commons Attribution 3.0 Unported Licence.

Fig. 1 Local PFM box-in-box (a) amplitude and (b) phase contrast images and PFM (c) amplitude, and (d) phase hysteresis loops of the 3 nm-thick YHO_7 film on a $Pt/Ti/SiO_2/Si$ substrate.

Consequently, three-dimensional and cross-sectional schematic illustrations of the nanocrossbar $Ti/TiO_x/YHO_7/Pt$ FTJ structure are shown in Fig. 2c and d, respectively. The nanocrossbar FTJ consists of a YHO_7 layer sandwiched between a bottom semicircular Pt nanowire and a top Ti nanowire electrode.

TER effect of nanocrossbar FTJs

Current (I)–voltage (V) hysteresis loops of a 3 nm-thick YHO_7 nanocrossbar FTJ with an area of 896 nm^2 (32 × 28 nm) were measured at room temperature (300 K) and 9 K (Fig. 3a). Typical I–V characteristic loops of 3 and 2 nm thick YHO7 nanocrossbar FTJs between 255 and 42 000 nm^2 at room temperature are shown in Fig. S3 and S4, respectively (SI).

It is noted that the shape and the current values of the I–V hysteresis loop at 300 K are almost the same as those at 9 K. When switching from OFF to ON at a positive voltage, the transition occurred abruptly. In contrast, the ON-to-OFF transition occurred gradually with increasing negative applied voltage. The coercive voltages from the OFF-to-ON transition were 1.6 and 1.8 V at 300 and 9 K, respectively, and those from the ON-to-OFF gradual transition were −1.0 to −1.3 V (300 K) and −1.2 to −1.8 V (9 K). The magnified I–V characteristics in the ON and OFF states are shown in the inset of Fig. 3a, where the current was approximately proportional to the voltage at 300 and 9 K. As the ON and OFF currents at 9 K are practically equal to those at 300 K and are proportional to voltage, the FTJ operation utilizes direct tunneling, which is highly dependent on the polarization direction.[13]

To further clarify the conduction mechanism, we analyzed the I–V characteristics of both the ON and OFF states in the intermediate voltage region ($V < \phi/e$), where ϕ is the tunneling barrier height and e is the elementary charge, using the Simmons direct tunneling model.[41] As shown in Fig. S5, the theoretical curves calculated using the Simmons equation are in excellent agreement with the experimental data for both re-

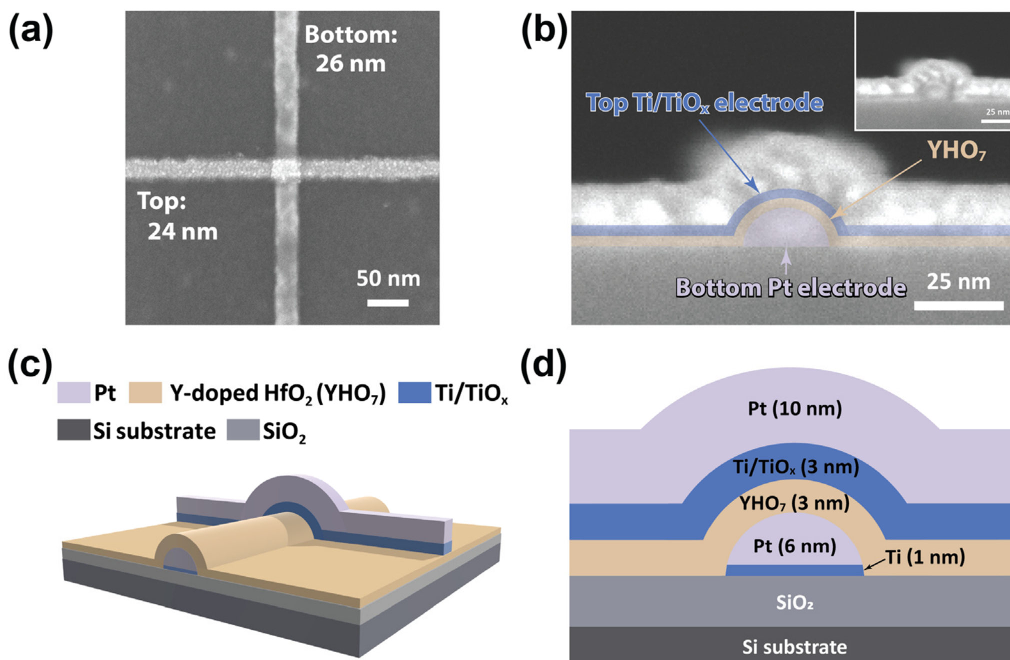

Fig. 2 (a) Top-view SEM image of a nanocrossbar $Ti/TiO_x/YHO_7$ (3 nm)/Pt ferroelectric tunnel junction (FTJ) with an area of 624 nm^2 (26 × 24 nm). (b) Cross-sectional SEM image of the $Ti/YHO_7/Pt$ structure with false coloring to highlight the Ti/TiO_x (blue), YHO_7 (light ochre), and Pt (purple) layers. The original image is shown at the top-right inset. For this cross-sectional view, the top Ti and Pt electrodes are successively deposited as continuous films rather than as nanowires. (c) 3D schematic and (d) cross-sectional schematics of the nanocrossbar $Ti/TiO_x/YHO_7/Pt$ FTJ.

Open Access Article. Published on 02 ledna 2026. Downloaded on 21.05.2026 4:19:18.
This article is licensed under a Creative Commons Attribution 3.0 Unported Licence.

sistance states. The fitting parameters were ϕ = 1.7 eV, d = 3.00 nm, and m^* = 0.3 m_0 for the low-resistance state (LRS), and ϕ = 1.7 eV, d = 3.48 nm, and m^* = 0.3 m_0 for the high-resistance state (HRS), where d is the tunneling barrier thickness, m^* is the electron effective mass, and m_0 is the mass of electron. The identical barrier height and effective mass for both states, together with the small difference in the effective barrier thickness of only 0.48 nm, indicate that the change in the depletion layer width at the TiO_x/YHO_7 interface governs the resistance switching. These results unambiguously confirm that electron transport in both resistance states is dominated by direct tunneling through the ultrathin YHO_7-based ferroelectric barrier.

The resistance–voltage (R–V) hysteresis loops were measured using the pulse sequence illustrated in Fig. 3b. Fig. 3c shows the R–V hysteresis loops of the same 3 nm-thick YHO_7 nanocrossbar FTJ with 896 nm^2 at 300 K and 9 K. This R–V hysteresis loop of the FTJ shows well-defined memory characteristics. The R–V hysteresis loop exhibits abrupt OFF-to-ON and gradual ON-to-OFF transition, which are consistent with the I–V hysteresis loops. The coercive voltages for the OFF-to-ON transition are 1.2 V at both 300 and 9 K. In comparison, those for the ON-to-OFF transition are −1.2 V at 300 K and −1.4 V at 9 K. These results indicate that the OFF-to-ON switching is relatively insensitive to temperature. In contrast, the ON-to-OFF switching becomes slightly harder at lower temperatures.

The asymmetric resistive-switching behavior observed in the $Ti/TiO_x/YHO_7/Pt$ nanocrossbar FTJ should arise from multiple interfacial and structural factors. First, the asymmetric electrode configuration produces different interface barrier heights due to the work-function difference between the Ti/TiO_x (≈4.3 eV) and Pt (≈5.6 eV) electrodes. This difference generates a built-in electric field across the junction, leading to asymmetric barrier modulation during switching.[42–44] Under positive bias (OFF-to-ON transition), the built-in field assists polarization reversal by lowering the effective tunneling barrier at the Ti/TiO_x interface, leading to a sharp increase in current. In contrast, under negative bias (ON-to-OFF transition), the field opposes polarization reversal, leading to a gradual decrease in current.

In addition to the work-function-induced barrier asymmetry, the nonplanar, curved surface geometry of the nanocrossbar FTJ further enhances the asymmetry. Because the YHO_7 thin film conforms to the semicircular Pt nanowire electrode, strain gradients naturally develop along the film thickness, inducing flexoelectric polarization.[45,46] The resulting flexoelectric field modifies the local electric potential, facilitating polarization nucleation during the OFF-to-ON process and stabilizing residual polarization during the ON-to-OFF transition. Consequently, the observed asymmetric I–V characteristics arise from the combined effects of the work-function-driven built-in field, the flexoelectric response associated with the curved device geometry, and the local domain-wall pinning.

This combined mechanism is consistent with the experimentally observed sharp ON-switching transition and gradual OFF-switching decay. These findings provide a comprehensive physical picture that explains the bias-polarity-dependent

This journal is © The Royal Society of Chemistry 2026

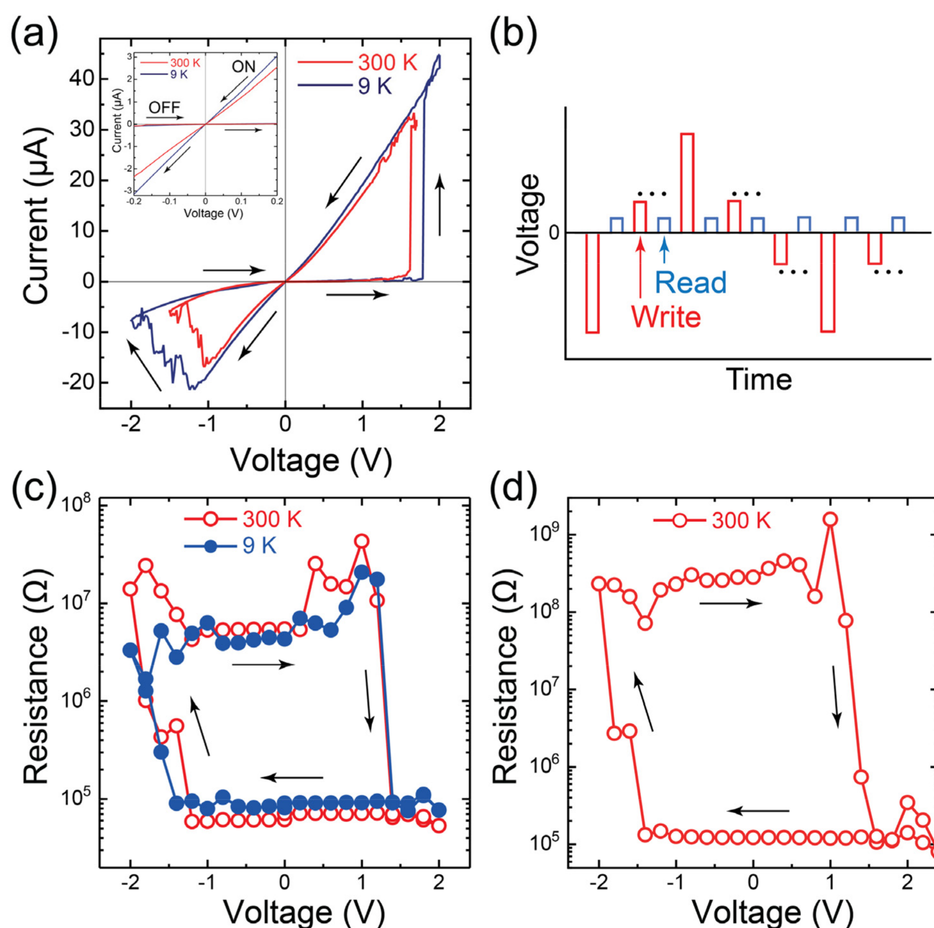

Fig. 3 Switching behaviors of 3 nm-thick YHO_7 nanocrossbar FTJs. (a) Temperature dependence of *I*–*V* hysteresis loops with an area of almost 30 nm squared (896 nm^2) at 300 K (red solid line) and 9 K (blue solid line). The magnified *I*–*V* characteristics under ON and OFF states (top left inset). (b) The pulse sequence for the *R*–*V* hysteresis loop. The write and read voltage widths are 200 ms and the read voltage is 0.1 V. (c) Temperature dependence of *R*–*V* hysteresis loops at 300 K (red open circle) and 9 K (blue closed circle) of the FTJ in (a) (30 nm squared). (d) *R*–*V* hysteresis loop of the 3 nm-thick YHO_7 nanocrossbar FTJ with 25 nm squared (624 nm^2) at 300 K.

Open Access Article. Published on 02 ledna 2026. Downloaded on 21.05.2026 4:19:18.
This article is licensed under a Creative Commons Attribution 3.0 Unported Licence.

asymmetry in the tunneling characteristics of the nanocrossbar FTJ.

As shown in Fig. 3c, the resistance values of the LRS and HRS are 7.8×10^4 Ω and 5.5×10^6 Ω at 300 K, and 8.9×10^4 Ω and 4.3×10^6 Ω at 9 K, respectively. The corresponding TER ratios of the 3 nm-thick YHO_7 nanocrossbar FTJ with 896 nm^2 at 300 K and 9 K are 71 and 48, respectively. It is noted that the resistance ratios between 300 K and 9 K under the LRS and HRS are 1.1 and 0.8, respectively, indicating minimal change in resistance despite the significant temperature difference, suggesting that transport is dominated by tunneling conduction with only a minor contribution from thermally activated processes. Compared with previously reported $BaTiO_3$- or HfO_2-based FTJs, where the OFF-state resistance generally shows a stronger temperature dependence due to trap-assisted or thermionic conduction,[13] the present YHO_7 nanocrossbar FTJ exhibits a remarkably weaker temperature dependence, highlighting the advantage of stabilized tunneling transport in this nanocrossbar FTJ.

Fig. 3d shows an *R*–*V* hysteresis loop of a 3 nm-thick YHO_7 nanocrossbar FTJ with 25 nm squared area (624 nm^2) at 300 K. The *R*–*V* hysteresis loop exhibits well-defined memory characteristics. The resistances of the LRS and HRS are 8.9×10^4 Ω and 4.3×10^6 Ω, respectively, yielding a TER ratio of 2.2×10^3. This TER ratio of 2.2×10^3 is more than one order of magnitude higher than that of the 30 nm crossbar device (TER = 71 at 300 K) as shown in Fig. 3c, indicating that device scaling substantially enhances the tunneling electroresistance effect. In the present 25 nm squared nanocrossbar FTJ, the transports under the LRS and HRS are clearly dominated by direct tunneling conduction, as evidenced by the extremely weak temperature dependence of both LRS and HRS. However, thermally activated processes significantly contributed to the HRS in previous reports.[13,34,35,47,48]

As observed in the *R*–*V* hysteresis loops in Fig. 3c and d, resistance gradually increases from ON to OFF and resistance abruptly decreases from OFF to ON, aligning well with the *I*–*V* hysteresis loops as shown in Fig. 3a.

The coercive voltages at 300 K are evaluated as −1.4 V from ON-to-OFF and 1.0 V from OFF-to-ON from the *R*–*V* hysteresis loop in Fig. 3d, which agrees with the coercive voltages given in Fig. 3c (−1.2 and 1.0 V, respectively). The average coercive electric field is calculated to be 4.0 MV cm^{-1} (1.2 V across 3 nm), which is in good agreement with our previous report (~4.3 MV cm^{-1}).[49,50]

The coercive voltages at 9 K are also evaluated as −1.4 V from ON to OFF and 1.2 V from OFF to ON, as indicated by the *R*–*V* hysteresis loop in Fig. 3c. These small temperature dependencies of the coercive voltages of the ON and OFF states at 300 K and 9 K agree well with the stable ferroelectricity and coercivity of the wake-up-free $Hf_{0.5}Zr_{0.5}O_2$ thin film over a wide temperature range from room temperature (300 K) to cryogenic temperature (30 K).[51] The temperature independence of resistance states also proves the TER effect on the 3 nm-thick YHO_7 nanocrossbar FTJ based on polarization switching.

Fig. 4a and b show the band diagrams of the ON (LRS) and OFF (HRS) states of the nanocrossbar FTJ with a junction structure of Ti/TiO_x (top electrode)/YHO_7/Pt (bottom electrode) in the opposite spontaneous polarization directions of YHO_7, respectively. At the Ti/YHO_7 interface, Ti scavenges oxygen from YHO_7, and Ti is partially oxidized at the interface, forming a Ti/TiO_x/YHO_7 structure at room temperature.[52–54] M. Sowinska *et al.* reported a TiO_x thickness of 1.3 nm at the Ti/HfO_2 interface based on X-ray reflection (XRR) and scanning transmission electron microscopy (STEM) with energy-dispersive X-ray spectroscopy (EDX) measurements.[52] The spontaneous polarization induces bound charges at the interfaces of the YHO_7 thin film, which are compensated at the top Ti/TiO_x and bottom Pt electrodes. In Pt, the screening effect is essentially polarity-independent owing to the large, nearly symmetric density of states near the Fermi level. In contrast, as TiO_x is an n-type semiconductor, when the polarization is pointing to the Ti/TiO_x side (Fig. 4(a)), electrons accumulate at the TiO_x surface. Then, the effective barrier height decreases, and the direct tunneling barrier width becomes the thickness of YHO_7, resulting in the LRS. On the other hand, when the polarization is pointing to the Pt side, positive charges are induced at the TiO_x/YHO_7 interface and electrons are depleted at the TiO_x surface. This results in both the effective tunnel barrier height and tunneling distance increasing owing to the depletion layer (HRS).

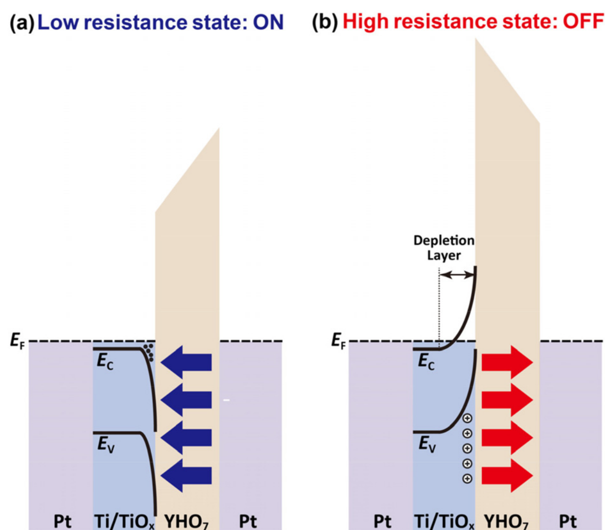

Fig. 4 Energy band diagrams of FTJs in (a) ON (LRS), and (b) OFF (HRS) states. In the LRS (a), the polarization is pointing to the Ti/TiO_x side and accumulates electrons at the TiO_x surface. In the HRS (b), the polarization is pointing to the Pt side and depletes electrons at the TiO_x surface, which makes the effective tunnel barrier width increase.

Compared with conventional metal/HfO_2-based ferroelectric/SiO_x/Si structures,[47] the Ti/TiO_x/YHO_7/Pt junction exhibits several advantages. First, the metal/ferroelectric/metal configuration eliminates the need for a SiO_x interlayer, which can lead to interface charge. Second, the polarity-dependent interfacial response at the TiO_x/YHO_7 contact enables a well-defined modulation of the tunneling barrier, resulting in a large ON/OFF ratio, as shown in Fig. 3. YHO_7 with high crystallinity can be directly grown on the Pt surface by sputtering at room temperature, thereby suppressing leakage paths that are often present in HfO_2/SiO_x/Si devices. Finally, the CMOS-compatible YHO_7 and scalable metal/ferroelectric/metal geometry make the TiO_x/YHO_7/Pt structure a promising platform for high-density non-volatile memory.

The abrupt decrease in resistance from the OFF to ON state and the gradual increase in resistance from the ON to OFF state in the *R*–*V* and *I*–*V* results (Fig. 3) arise from distinct polarization-switching processes.[55] During the ON to OFF transition, domain-wall pinning provides pre-existing nucleation sites, facilitating gradual polarization reversal under an increasing electric field. In contrast, the OFF-to-ON transition requires the activation of new nucleation centers, leading to an abrupt polarization-switching event. Such asymmetric switching behavior is consistent with previous reports of defect-mediated pinning in HfO_2-based FTJs, in which oxygen vacancies and hydrogen-related complexes hinder polarization reversal until passivation treatments are applied.[56] Interface-induced pinning due to oxygen-vacancy segregation and electrode scavenging has also been shown to significantly affect the TER.[57] In addition, direct spectroscopic evidence of domain-wall pinning in ferroelectric HfO_2 thin films supports our interpretation that domain-wall pinning acts as a nucleation source during gradual ON to OFF switching.[58]

It is noted that these asymmetrical resistance-switching behaviors were observed in the nanocrossbar FTJ area of 896 nm^2. The gradual resistance transition from the ON to OFF state suggests a self-polarization reversal with a gradual domain growth process even in the small FTJ area of 896 nm^2. An abrupt transition from OFF to ON in resistance suggests simultaneous self-polarization switching across all domains within the crossbar FTJ at 896 nm^2. This nanocrossbar FTJ opens up possibilities for advanced multi-state memory applications, leveraging domain-forming mechanisms and asymmetrical resistance-switching behavior in small FTJ areas.[59]

Open Access Article. Published on 02 ledna 2026. Downloaded on 21.05.2026 4:19:18.
This article is licensed under a Creative Commons Attribution 3.0 Unported Licence.

This journal is © The Royal Society of Chemistry 2026

Open Access Article. Published on 02 ledna 2026. Downloaded on 21.05.2026 4:19:18.
This article is licensed under a Creative Commons Attribution 3.0 Unported Licence.

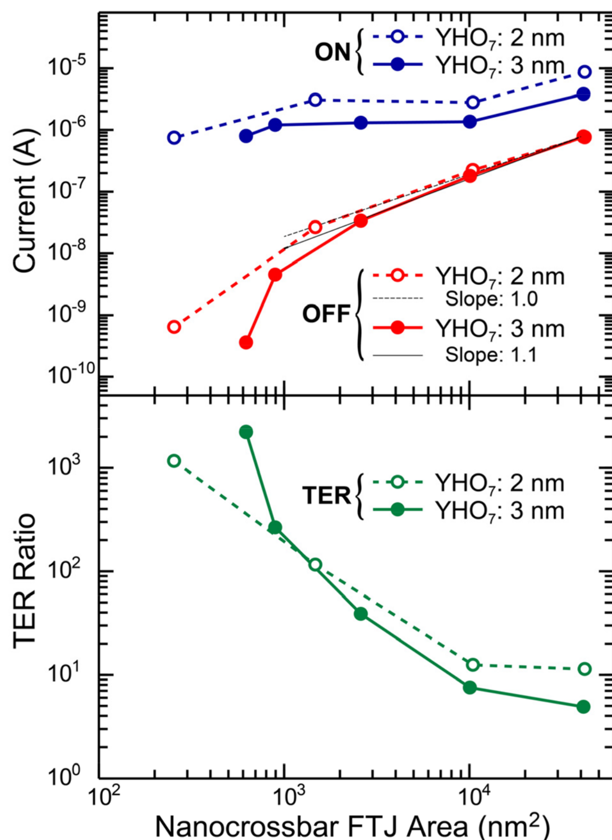

Fig. 5 Nanocrossbar FTJ area dependence of I_{ON}, I_{OFF} (upper), and TER ratio (lower) for 2 nm and 3 nm-thick YHO_7. Read voltage is 0.1 V.

Nanocrossbar FTJ area dependence of the TER effect

The nanocrossbar FTJ area dependence of the ON current (I_{ON}), OFF current (I_{OFF}), and TER ratio is shown in Fig. 5 for nanocrossbar FTJs with YHO_7 thicknesses of 2 and 3 nm. The read currents were measured at 0.1 V. Both I_{OFF} and I_{ON} decreased with decreasing nanocrossbar FTJ area from 42 000 nm^2 to 255 nm^2 (2 nm-thick YHO_7) and 624 nm^2 (3 nm-thick YHO_7). The I_{OFF} and I_{ON} slopes relative to the FTJ area are calculated as shown in Fig. 5.

For the I_{OFF} of nanocrossbar FTJs, the slopes with the reduction of FTJ area are 1.0 (black dotted line) and 1.1 (black solid line) between 42 000 and 1476 nm^2 (2 nm-thick YHO_7), and between 41 370 and 2597 nm^2 (3 nm-thick YHO_7), respectively. It is noted that the I_{OFF} slope values of approximately 1 follow Ohm's law, in which the resistance is inversely proportional to the area. When the FTJ area is less than 1476 nm^2 (2 nm-thick YHO_7) and 2597 (3 nm-thick YHO_7), I_{OFF} decreases more rapidly with area, and the slopes are 2.4 and 3.0 between 1476 and 255 nm^2, and between 2597 and 624 nm^2, respectively.

To examine the device-to-device consistency, several nanocrossbar $Ti/TiO_x/YHO_7/Pt$ FTJs with identical lateral dimensions of 50 × 50 nm^2 were characterized and are summarized in the SI (Fig. S6). I_{ON} and I_{OFF}, as well as the resulting TER ratios, were found to be nearly identical among all measured devices, indicating good reproducibility and uniformity of the switching behavior. These results suggest that uniform ferroelectric switching behavior is maintained even in 3 nm-thick YHO_7 films where multiple structural phases may coexist.

McKenna *et al.* reported grain boundary-mediated leakage current in polycrystalline 5 nm HfO_2 thin films grown on p-type Si with a 1 nm-thick native SiO_2 layer, using conductive atomic force microscopy with a 6.5 V conductive tip voltage (resulting in p-type Si depletion).[60] It was concluded that the tunneling barrier is lowered at grain boundaries as a result of their intrinsic electronic properties and that leakage current tends to dominate grain boundaries.[60] The grain boundary length should be proportional to the FTJ area. When the grain size is smaller than the FTJ area, leakage paths at the grain boundary should be proportional to the FTJ area. The more rapid decreasing I_{OFF} compared with the theoretical change with decreasing YHO_7 nanocrossbar FTJ area should be attributed to the reduced defect-induced leakage paths, such as grain-boundary-induced leakage paths with a reduced FTJ area when minimizing FTJ size smaller than 2500 nm^2.[60]

This interpretation is corroborated by microscopic structural analysis. Cross-sectional BF-TEM and EDS elemental mapping (Fig. S1 and S2) reveal that the 2–3 nm-thick YHO7 film is conformally grown on the semicircular Pt nanowire electrode and does not exhibit extended columnar grains. High-resolution TEM further confirms that the smallest nanocrossbar junctions (25 nm in width) correspond to a single-grain or partially single-grain region of YHO_7. Therefore, continuous grain-boundary networks capable of forming leakage paths are absent at this scale, consistent with the rapid suppression of I_{OFF} in the smallest devices.

For the I_{ON} of nanocrossbar FTJs, the slopes were 0.41 (2 nm-thick YHO_7) and 0.30 (3 nm-thick YHO_7) in the range of FTJ area between 42 000 and 255 nm^2 and between 41 370 and 624 nm^2, respectively. These sub-linear slopes (<1) of I_{ON} indicate that the effective fraction of the active direct tunneling region for I_{ON} increases as the FTJ area decreases, reflecting the enhancement of the curved nanocrossbar geometry on the direct-tunneling area.

Boyn *et al.* reported that the ratio of effective switching domain area to FTJ area increases as the $BiFeO_3$ area is reduced from 1.13 μm^2 to 25 400 nm^2, leading to improved uniformity of remanent polarization.[61] With decreasing FTJ area, the number of activated nucleation centers to turn the FTJ from the OFF state to the ON state should become small, and electrons at the Ti/TiO_x interface should more uniformly accumulate at the whole nanocrossbar FTJ area. As a result, with the decreasing FTJ area, I_{ON} did not decrease below the theoretical slope of 1 due to more uniform domain switching.[61]

In Fig. 5, for the nanocrossbar FTJ with 2 nm-thick YHO_7, with the decrease of FTJ area from 42 000 to 255 nm^2, I_{ON} decreases from 8.7 μA to 0.75 μA, and I_{OFF} decreases from 0.77 μA to 0.63 nA, respectively, resulting in an elevation of the TER ratio from 11 to 1.2×10^3. For a 3 nm-thick YHO_7

nanocrossbar FTJ, with the decrease of FTJ area from 41 270 to 624 nm^2, I_{ON} decreases from 3.8 μA to 0.80 μA, and I_{OFF} decreases from 0.78 μA to 0.36 nA, respectively, resulting in an elevation of the TER ratio from 4.9 to 2.2×10^3. It is noted that the ideal nanocrossbar FTJ area dependencies of I_{ON}, I_{OFF}, and TER ratio have been observed for both YHO_7 thicknesses of 2 and 3 nm. Consequently, a TER ratio of 2.2×10^3 has been obtained on the nanocrossbar FTJ at the smallest area of 624 nm^2 on 3 nm-thick YHO_7 under the direct tunneling regime, even at the HRS.

In most previously reported $BaTiO_3$- and HfO_2-based FTJs, the TER ratios at room temperature are typically in the range of $10–10^3$, which is comparable to the case of the present nanocrossbar Ti/TiO_x/YHO_7/Pt FTJs exhibiting a TER of 2×10^3. Although much higher TER ratios up to 10^7 have been reported for HfO_2-based FTJs such as HZO/Nb (0.7 wt%)-doped $SrTiO_3$ (NSTO) heterojunctions, the huge resistance contrast in those systems primarily originates from the depletion region formed in the n-type NSTO semiconductor, which strongly suppresses the OFF-state current.[10,48] In our Ti/TiO_x/YHO_7/Pt nanocrossbar FTJs, a depletion layer may also form to some extent at the n-type TiO_x interface; however, both the ON and OFF currents are governed by direct tunneling through the ultrathin YHO_7 barrier. This high-resistance-state tunneling behavior is supported by the observation that the ON- and OFF-state current levels and TER ratios remain nearly identical at 9 K and 300 K. Accordingly, the observed TER ratio of 2×10^3 represents a realistic value for intrinsic polarization-controlled tunneling in a metallic nanocrossbar FTJ, free from additional semiconductor depletion effects.

Open Access Article. Published on 02 ledna 2026. Downloaded on 21.05.2026 4:19:18.
This article is licensed under a Creative Commons Attribution 3.0 Unported Licence.

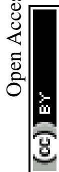

Retention characteristics

Retention characteristics of 3 nm-thick YHO_7 nanocrossbar FTJs with 896 (32 × 28) nm^2 are shown in Fig. 6. The ON and OFF states were measured using the pulse sequence illustrated in the insets. Initially, a negative erase pulse voltage of −2 V was applied to the bottom Pt electrode, switching the nanocrossbar FTJ to the high-resistance OFF state. Subsequent continuous read pulses of 0.1 V confirmed a stable OFF-state resistance of 2×10^7 Ω maintained for up to 1000 s. A positive write pulse voltage of 2 V was then applied, switching the nanocrossbar FTJ to the ON-state. A stable ON-state resistance of 2×10^5 Ω was retained for 1000 s. The resulting TER ratio of approximately 100 is consistent with the data presented in Fig. 3c.

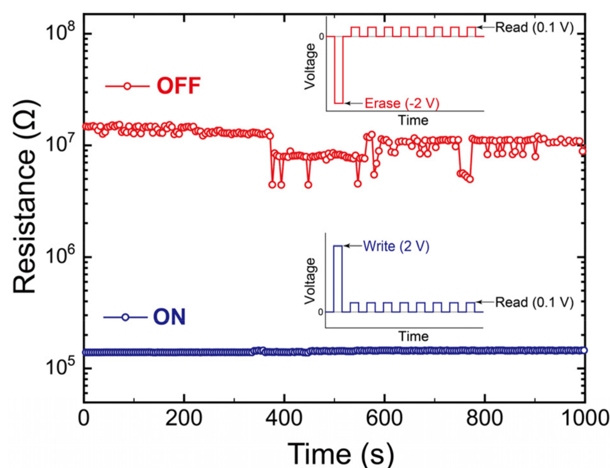

Fig. 6 Retention characteristics of the 3 nm-thick YHO_7 nanocrossbar FTJ with an area of 896 nm^2; the pulse sequences are shown in the inset. The write, erase, and read voltages are 2, −2, and 0.1 V, respectively. All write, erase, and read pulse widths are 200 ms.

To further clarify the retention behavior, the same dataset shown in Fig. 6 was replotted as linear resistance (R)–log time graphs and is provided in Fig. S7 (SI). The ON-state current remained remarkably stable, showing almost no change over the entire measurement period (up to 10^3 s), whereas the OFF-state resistance gradually decreased with time. Extrapolation of the linear R–log time plot suggests that the OFF-state resistance, and consequently the TER ratio, would decrease to approximately half of its initial value after 10 years (≈3.15×10^8 s). Nevertheless, a clear contrast in resistance between the ON and OFF states would still be maintained.

The switching reliability of the nanocrossbar Ti/TiO_x/YHO_7/Pt FTJs was evaluated by endurance measurements using a device with lateral dimensions of 50 × 50 nm^2 and a 3 nm-thick YHO_7 layer (Fig. S3). The device was repeatedly switched between the ON and OFF states by applying write and erase voltages of 2 V and −2 V, respectively, while the resistance was read at 0.1 V. The nanocrossbar FTJ exhibited stable and reproducible resistive switching without noticeable degradation, demonstrating that the device can withstand at least 100 consecutive switching operations (Fig. S8, SI). These retention and endurance characteristics suggest a robust long-term non-volatile functionality in nanocrossbar FTJ devices.

Conclusions

We demonstrated scalable nanocrossbar-type FTJs using a double-exposure EBL process. Nanocrossbar FTJs consisting of top Ti/TiO_x electrode/YHO_7/bottom Pt electrode on SiO_2/Si substrates were fabricated with lateral dimensions down to 25 nm. The temperature dependence of the TER effect at 9 and 300 K reveals direct tunneling conduction not only in the LRS but also in the HRS. A TER ratio of 2.2×10^3 was achieved in the 3 nm-thick YHO_7 nanocrossbar FTJ with a lateral dimension of 25 nm. Nanocrossbar FTJ area dependence of the TER effect coincides well with 3 and 2 nm-thick YHO_7. The OFF-state current decreased with a slope of 1.1 between 42 000 and 2597 nm^2, and then the slope became steeper below 2597 nm^2. In contrast, the ON-state current slowly reduced with a slope of 0.30. The large (>1.1) and small (0.30) slopes of the OFF and ON-state current showing nanocrossbar area dependence were discussed in terms of the suppression of leakage pathways along grain boundaries and uniformly aligned remanent polarization within a limited number of grains, respectively. The nanocrossbar FTJ is significant for high-density,

This journal is © The Royal Society of Chemistry 2026

energy-efficient, and CMOS-compatible integration of scalable ferroelectric memory.

Experimental methods

Scalable nanocrossbar FTJ fabrication

The bottom nanowire electrodes, made of Pt (6 nm)/Ti (1 nm), were fabricated using electron-beam lithography (ELS-7500EX, Elionix, Japan) and E-beam evaporation, followed by a lift-off process. The linewidth of the Pt nanowires was designed using CAD software for EBL. The bottom Pt electrodes were then annealed in a 3% H_2/Ar mixture for 5 min at 550 °C. As shown in the SEM image (Fig. 2b), the cross-sectional shape of the bottom Pt electrode deformed from a rectangle to a semicircular arch, known as Rayleigh instability, to reduce surface free energy and improve the crystallinity of the bottom Pt nanowire during the annealing.[39,40]

YHO_7 ultrathin films with thicknesses of 3 and 2 nm were deposited onto a bottom Pt/Ti nanowire and a SiO_2/Si substrate using RF magnetron sputtering with a 2-inch diameter YHO_7 ceramic target (Toshima Manufacturing, Japan).[31] The distance between the target surface and the substrate was 70 mm. Sputtering was carried out under a pure Ar atmosphere at a total pressure of 10 mTorr with an RF power of 50 W. No thermal treatment was applied to the YHO_7 thin film during sputtering or after deposition.

For the top Ti nanowire electrodes, Pt (10 nm)/Ti (3 nm) was deposited using a double-exposure EBL process followed by E-beam evaporation and a lift-off process. Uniform nanocrossbar Ti/TiO_x/YHO_7/Pt junctions were prepared as shown in the cross-sectional SEM image (Fig. 2(b)). Using a designed mask, the probing pads for the bottom and top Pt (40 nm)/Ti (5 nm) electrodes were fabricated by photolithography, E-beam evaporation, and a lift-off process.

Ferroelectric YHO_7 film characterization

PFM measurement of the ferroelectric 3 nm-thick YHO_7 thin film was carried out with an atomic force microscope (Asylum Research Cypher, Japan, MFP-3D scanning probe microscope) by using Pt/Ir-coated Si cantilever tips (NanoAndMore, USA, nominal spring constant 2.8 N m^{-1}). A bidirectional bias sweep between −15 V and 15 V was applied to measure hysteresis loops under Dual-Resonance Amplitude Tracking (DRAT) mode.[38]

Nanocrossbar FTJ switching property measurements

Electrical properties of nanocrossbar FTJs were measured using a mechanical helium refrigerator multi-probe (GRAIL10-LOGOS01S, Nagase, Japan) and a semiconductor parameter device analyzer (B1500, Keysight, USA). FTJ switching property measurement temperatures were 300 and 9 K. All measurements were conducted in a vacuum (≈10^{-4} Pa) and a dark environment. The temperature dependence of the current–voltage (I–V) hysteresis loop was measured by applying a triangular voltage waveform to the bottom Pt electrode at 0.02 Hz. The TER ratio was calculated from the current–voltage characteristics, defined as $(R_{OFF}–R_{ON})/R_{ON} \times 100\%$, where R_{OFF} and R_{ON} are the FTJ resistances for the OFF and ON states, respectively, at a voltage of 0.1 V.

As shown in Fig. 3b, the resistance–voltage (R–V) hysteresis loop was measured as follows: a negative write pulse of −2 V was first applied to the bottom Pt electrode, setting the junction to a high-resistance (OFF) state. Then, the read voltage was set to 0.1 V. Subsequently, positive voltage pulses were applied in steps from 0.2 V to 2 V (or 2.4 V) in 0.2 V increments. The voltage was then swept down from 2 (or 2.4) V to −2 V in −0.2 V steps, and finally increased back to 0 V. After each write pulse, a read pulse of 0.1 V was applied to probe the resistance. Both write and read pulses had widths of 200 ms.

After measuring the electrical properties, the nanocrossbar FTJs were characterized by FE-SEM (Regulus 8230, Hitachi High-Tech, Japan).

Author contributions

Y. M. conceived the research. Z. S. performed most of the FTJ device preparation and electrical measurements. Y. N., K. O., and H. F. helped in YHO_7 sputtering. Z. S., S. I., H. F., and Y. M. analyzed and discussed the experimental data. Z. S. and Y. M. wrote the manuscript.

Conflicts of interest

There are no conflicts to declare.

Data availability

Supplementary information (SI): detailed electrical characterization results. See DOI: https://doi.org/10.1039/d5nr04010h.

Acknowledgements

This study was partially supported by JST CREST (Grant No. JPMJCR22B4) and the MEXT Program: Data Creation and Utilization Type Material Research and Development (Grant No. JPMXP1122683430). H. F. thanks the MEXT Initiative to Establish Next-generation Novel Integrated Circuits Centers (X-NICS) (Grant No. JPJ011438), JST-Adopting Sustainable Partnerships for Innovative Research Ecosystem (ASPIRE) (Grant No. JPMJAP2312), and the Japan Society for the Promotion of Science (JSPS) KAKENHI (Grant No. 22K18307). Z. S. thanks JST SPRING (Grant No. JPMJSP2106). We also thank Ms. M. Miyakawa, Ms. I. Shimada, and Mr. D. Shoji, Institute of Science Tokyo, for their technical support.

Open Access Article. Published on 02 ledna 2026. Downloaded on 21.05.2026 4:19:18.
This article is licensed under a Creative Commons Attribution 3.0 Unported Licence.

Open Access Article. Published on 02 ledna 2026. Downloaded on 21.05.2026 4:19:18.
This article is licensed under a Creative Commons Attribution 3.0 Unported Licence.

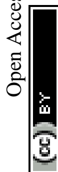

References

1 S. Yu, *Semiconductor Memory Devices and Circuits*, CRC Press, Boca Raton, 2022.
2 W. Banerjee, *Electronics*, 2020, **9**, 1029, DOI: 10.3390/electronics9061029.
3 T. Endoh, H. Koike, S. Ikeda, T. Hanyu and H. Ohno, *IEEE J. Emerg. Sel. Top. Circuits Syst.*, 2016, **6**, 109–119, DOI: 10.1109/JETCAS.2016.2547704.
4 B. Prasad, Y. Huang, R. V. Chopdekar, Z. Chen, J. Steffes, S. Das, Q. Li, M. Yang, C. Lin, T. Gosavi, D. E. Nikonov, Z. Q. Qiu, L. W. Martin, B. D. Huey, I. Young, J. Íñiguez, S. Manipatruni and R. Ramesh, *Adv. Mater.*, 2020, **32**, 2001943, DOI: 10.1002/adma.202001943.
5 S. Manipatruni, D. E. Nikonov and I. A. Young, *Nat. Phys.*, 2018, **14**, 338–343, DOI: 10.1038/s41567-018-0101-4.
6 S. Manipatruni, D. E. Nikonov, C.-C. Lin, T. A. Gosavi, H. Liu, B. Prasad, Y.-L. Huang, E. Bonturim, R. Ramesh and I. A. Young, *Nature*, 2019, **565**, 35–42, DOI: 10.1038/s41586-018-0770-2.
7 S. Oh, H. Hwang and I. K. Yoo, *APL Mater.*, 2019, **7**, 091109, DOI: 10.1063/1.5108562.
8 N. A. Spaldin and R. Ramesh, *Nat. Mater.*, 2019, **18**, 203–212, DOI: 10.1038/s41563-018-0275-2.
9 Z. Wang, H. Wu, G. W. Burr, C. S. Hwang, K. L. Wang, Q. Xia and J. J. Yang, *Nat. Rev. Mater.*, 2020, **5**, 173–195, DOI: 10.1038/s41578-019-0159-3.
10 S. H. Park, H. J. Lee, M. H. Park, J. Kim and H. W. Jang, *J. Phys. D: Appl. Phys.*, 2024, **57**, 253002, DOI: 10.1088/1361-6463/ad33f5.
11 M. H. Park, H. J. Kim, Y. J. Kim, Y. H. Lee, T. Moon, K. Do Kim, S. D. Hyun, F. Fengler, U. Schroeder and C. S. Hwang, *ACS Appl. Mater. Interfaces*, 2016, **8**, 15466–15475, DOI: 10.1021/acsami.6b03586.
12 P. Maksymovych, S. Jesse, P. Yu, R. Ramesh, A. P. Baddorf and S. V. Kalinin, *Science*, 2009, **324**, 1421–1425, DOI: 10.1126/science.1171200.
13 J. Hwang, Y. Goh and S. Jeon, *Small*, 2024, **20**, 2305271, DOI: 10.1002/smll.202305271.
14 Z. Wen and D. Wu, *Adv. Mater.*, 2020, **32**, 1904123, DOI: 10.1002/adma.201904123.
15 L. Esaki, R. B. Laibowitz and P. J. Stiles, *IBM Tech. Disc. Bull.*, 1971, **13**, 2161.
16 H. Qiao, C. Wang, W. S. Choi, M. H. Park and Y. Kim, *Mater. Sci. Eng. R Rep.*, 2021, **145**, 100622, DOI: 10.1016/j.mser.2021.100622.
17 S. Li, J. A. Eastman, J. M. Vetrone, C. M. Foster, R. E. Newnham and L. E. Cross, *Jpn. J. Appl. Phys.*, 1997, **36**, 5169, DOI: 10.1143/JJAP.36.5169.
18 V. M. Fridkin, S. Ducharme, A. V. Bune, S. P. Palto, S. G. Yudin and L. M. Blinov, *Ferroelectrics*, 2000, **236**, 1–10, DOI: 10.1080/00150190008016036.
19 A. Gruverman, D. Wu, H. Lu, Y. Wang, H. W. Jang, C. M. Folkman, M. Ye. Zhuravlev, D. Felker, M. Rzchowski, C.-B. Eom and E. Y. Tsymbal, *Nano Lett.*, 2009, **9**, 3539–3543, DOI: 10.1021/nl901754t.
20 J. Rodríguez Contreras, H. Kohlstedt, U. Poppe, R. Waser, C. Buchal and N. A. Pertsev, *Appl. Phys. Lett.*, 2003, **83**, 4595–4597, DOI: 10.1063/1.1627944.
21 W. Xiao, X. Zheng, H. Hao, L. Kang, L. Zhang and Z. Zeng, *npj Comput. Mater.*, 2023, **9**, 144, DOI: 10.1038/s41524-023-01101-9.
22 Z. Wang, W. Zhao, A. Bouchenak-Khelladi, Y. Zhang, W. Lin, J.-O. Klein, D. Ravelosona and C. Chappert, *J. Phys. D:Appl. Phys.*, 2013, **47**, 045001, DOI: 10.1088/0022-3727/47/4/045001.
23 J. Müller, T. S. Böscke, D. Bräuhaus, U. Schröder, U. Böttger, J. Sundqvist, P. Kücher, T. Mikolajick and L. Frey, *Appl. Phys. Lett.*, 2011, **99**, 112901, DOI: 10.1063/1.3636417.
24 G. D. Wilk, R. M. Wallace and J. M. Anthony, *J. Appl. Phys.*, 2001, **89**, 5243–5275, DOI: 10.1063/1.1361065.
25 T. S. Böscke, J. Müller, D. Bräuhaus, U. Schröder and U. Böttger, *Appl. Phys. Lett.*, 2011, **99**, 102903, DOI: 10.1063/1.3634052.
26 M. H. Park, Y. H. Lee, H. J. Kim, Y. J. Kim, T. Moon, K. Do Kim, J. Müller, A. Kersch, U. Schroeder, T. Mikolajick and C. S. Hwang, *Adv. Mater.*, 2015, **27**, 1811–1831, DOI: 10.1002/adma.201404531.
27 M. Dogan, N. Gong, T.-P. Ma and S. Ismail-Beigi, *Phys. Chem. Chem. Phys.*, 2019, **21**, 12150–12162, DOI: 10.1039/C9CP01880H.
28 S. K. Lee and C. W. Bark, *J. Korean Ceram. Soc.*, 2022, **59**, 25–43, DOI: 10.1007/s43207-021-00171-z.
29 J. Müller, T. S. Böscke, U. Schröder, S. Mueller, D. Brauhaus, U. Böttger, L. Frey and T. Mikolajick, *Nano Lett.*, 2012, **12**, 4318, DOI: 10.1021/nl302049k.
30 S. Shi, H. Xi, T. Cao, W. Lin, Z. Liu, J. Niu, D. Lan, C. Zhou, J. Cao, H. Su, T. Zhao, P. Yang, Y. Zhu, X. Yan, E. Y. Tsymbal, H. Tian and J. Chen, *Nat. Commun.*, 2023, **14**, 1780, DOI: 10.1038/s41467-023-37560-3.
31 T. Mimura, T. Shimizu, H. Uchida and H. Funakubo, *Appl. Phys. Lett.*, 2020, **116**, 062901, DOI: 10.1063/1.5140612.
32 Z. Wang, Z. Guan, H. Sun, Z. Luo, H. Zhao, H. Wang, Y. Yin and X. Li, *ACS Appl. Mater. Interfaces*, 2022, **14**, 24602–24609, DOI: 10.1021/acsami.2c04441.
33 X. S. Gao, J. M. Liu, K. Au and J. Y. Dai, *Appl. Phys. Lett.*, 2012, **101**, 142905, DOI: 10.1063/1.4756918.
34 A. Chanthbouala, A. Crassous, V. Garcia, K. Bouzehouane, S. Fusil, X. Moya, J. Allibe, B. Dlubak, J. Grollier, S. Xavier, C. Deranlot, A. Moshar, R. Proksch, N. D. Mathur, M. Bibes and A. Barthélémy, *Nat. Nanotechnol.*, 2012, **7**, 101–104, DOI: 10.1038/NNANO.2011.213.
35 M. Abuwasib, J.-W. Lee, H. Lee, C.-B. Eom, A. Gruverman and U. Singisetti, *J. Vac. Sci. Technol. B*, 2017, **35**, 021803, DOI: 10.1116/1.4978519.
36 Y. Y. Choi, T. Teranishi and Y. Majima, *Appl. Phys. Express*, 2019, **12**, 025002, DOI: 10.7567/1882-0786/aafb20.
37 S. Miao, R. Nitta, S. Izawa and Y. Majima, *Adv. Sci.*, 2023, **10**, 2370198, DOI: 10.1002/advs.202370198.
38 A. Gruverman and A. Kholkin, *Rep. Prog. Phys.*, 2006, **69**, 2443, DOI: 10.1088/0034-4885/69/8/R04.

 This journal is © The Royal Society of Chemistry 2026

Open Access Article. Published on 02 ledna 2026. Downloaded on 21.05.2026 4:19:18.
This article is licensed under a Creative Commons Attribution 3.0 Unported Licence.

39 R. Toyama, S. Kawachi, J. Yamaura, T. Fujita, Y. Murakami, H. Hosono and Y. Majima, *Nanoscale Adv.*, 2022, **4**, 5270–5280, DOI: 10.1039/D2NA00626J.
40 M. Zhao, R. Nitta, S. Izawa, J. Yamaura and Y. Majima, *Adv. Funct. Mater.*, 2025, **35**, 2415971, DOI: 10.1002/adfm.202415971.
41 J. G. Simmons, *J. Appl. Phys.*, 1963, **34**, 1793–1803, DOI: 10.1063/1.1702682.
42 E. Y. Tsymbal and H. Kohlstedt, *Science*, 2006, **313**, 181–183, DOI: 10.1126/science.1126230.
43 M. Y. Zhuravlev, R. F. Sabirianov, S. S. Jaswal and E. Y. Tsymbal, *Phys. Rev. Lett.*, 2005, **94**, 246802, DOI: 10.1103/PhysRevLett.94.246802.
44 V. Garcia, M. Bibes, L. Bocher, S. Valencia, F. Kronast, A. Crassous, X. Moya, S. Enouz-Vedrenne, A. Gloter, D. Imhoff, C. Deranlot, N. D. Mathur, S. Fusil, K. Bouzehouane and A. Barthélémy, *Science*, 2010, **327**, 1106–1110, DOI: 10.1126/science.1184028.
45 G. Catalan, A. Lubk, A. H. G. Vlooswijk, E. Snoeck, C. Magen, A. Janssens, G. Rispens, G. Rijnders, D. H. A. Blank and B. Noheda, *Nat. Mater.*, 2011, **10**, 963–967, DOI: 10.1038/NMAT3141.
46 J. Narvaez, S. Saremi, J. Hong, M. Stengel and G. Catalan, *Phys. Rev. Lett.*, 2015, **115**, 037601, DOI: 10.1103/PhysRevLett.115.037601.
47 K. Lee, J. Byun, K. Park, S. Kang, M. S. Song, J. Park, J. Lee and S. C. Chae, *Appl. Mater. Today*, 2022, **26**, 101308, DOI: 10.1016/j.apmt.2021.101308.
48 Z. Gao, W. Zhang, Q. Zhong, Y. Zheng, S. Lv, Q. Wu, Y. Song, S. Zhao, Y. Zheng, T. Xin, Y. Wang, W. Wei, X. Ren, J. Yang, C. Ge, J. Tao, Y. Cheng and H. Lyu, *Device*, 2023, **1**, 100004, DOI: 10.1016/j.device.2023.100004.
49 B. Prasad, V. Thakare, A. Kalitsov, Z. Zhang, B. Terris and R. Ramesh, *Adv. Electron Mater.*, 2021, **7**, 2001074, DOI: 10.1002/aelm.202001074.
50 H. Wang, Z. Guan, J. Li, Z. Luo, X. Du, Z. Wang, H. Zhao, S. Shen, Y. Yin and X. Li, *Adv. Mater.*, 2024, **36**, 2211305, DOI: 10.1002/adma.202211305.
51 S. Wu, R. Cao, H. Jiang, Y. Li, X. Zhang, Y. Yang, Y. Wang, Y. Wei and Q. Liu, *J. Semicond*, 2024, **45**, 032301, DOI: 10.1088/1674-4926/45/3/032301.
52 M. Sowinska, T. Bertaud, D. Walczyk, S. Thiess, M. A. Schubert, M. Lukosius, W. Drube, Ch. Walczyk and T. Schroeder, *Appl. Phys. Lett.*, 2012, **100**, 233509, DOI: 10.1063/1.4728118.
53 P. Calka, M. Sowinska, T. Bertaud, D. Walczyk, J. Dabrowski, P. Zaumseil, C. Walczyk, A. Gloskovskii, X. Cartoixa, J. Suñé and T. Schroeder, *ACS Appl. Mater. Interfaces*, 2014, **6**, 5056–5060, DOI: 10.1021/am500137y.
54 M. Pešić, F. P. G. Fengler, L. Larcher, A. Padovani, T. Schenk, E. D. Grimley, X. Sang, J. M. LeBeau, S. Slesazeck, U. Schroeder and T. Mikolajick, *Adv. Func. Mater.*, 2016, **26**, 4601, DOI: 10.1002/adfm.201600590.
55 A. Chanthbouala, V. Garcia, R. O. Cherifi, K. Bouzehouane, S. Fusil, X. Moya, S. Xavier, H. Yamada, C. Deranlot, N. D. Mathur, M. Bibes, A. Barthélémy and J. Grollier, *Nat. Mater.*, 2012, **11**, 860–864, DOI: 10.1038/NMAT3415.
56 M.-C. Nguyen, K. K. Min, W. Shin, J. Yim, R. Choi and D. Kwon, *Nano Convergence*, 2025, **12**, 17, DOI: 10.1186/s40580-025-00481-6.
57 N. Tasneem, H. Kashyap, K. Chae, C. Park, P.-C. Lee, S. F. Lombardo, N. Afroze, M. Tian, H. Kumarasubramanian, J. Hur, H. Chen, W. Chern, S. Yu, P. Bandaru, J. Ravichandran, K. Cho, J. Kacher, A. C. Kummel and A. I. Khan, *ACS Appl. Mater. Interfaces*, 2022, **14**, 43897, DOI: 10.1021/acsami.2c11736.
58 R. Marquardt, D. Petersen, O. Gronenberg, F. Zahari, R. Lamprecht, G. Popkirov, J. Carstensen, L. Kienle and H. Kohlstedt, *ACS Appl. Electron. Mater.*, 2023, **5**, 3251–3260, DOI: 10.1021/acsaelm.3c00336.
59 M. D. Henry, D. Stoltzfus, M. K. Lenox, S. T. Jaszewski, T. Young and J. F. Ihlefeld, *J. Appl. Phys.*, 2025, **137**, 144104, DOI: 10.1063/5.0256686.
60 K. McKenna, A. Shluger, V. Iglesias, M. Porti, M. Nafría, M. Lanza and G. Bersuker, *Microelectron. Eng.*, 2011, **88**, 1272–1275, DOI: 10.1016/j.mee.2011.03.024.
61 S. Boyn, A. M. Douglas, C. Blouzon, P. Turner, A. Barthélémy, M. Bibes, S. Fusil, J. M. Gregg and V. Garcia, *Appl. Phys. Lett.*, 2016, **109**, 232902, DOI: 10.1063/1.4971311.